Partitioning of Solute to the Primary α-Mg Phase in Creep-Resistant Mg-Al-Ca–Based Cast Alloys

JESSICA R. TERBUSH, NICHOLAS D. SADDOCK, J. WAYNE JONES, and TRESA M. POLLOCK

The partitioning of elements during solidification of ternary and quaternary Mg-Al-Ca alloys has been measured by an electron microprobe segregation mapping technique. Differences in the degree of partitioning of Al and Ca to the α-Mg phase in as-solidified MRI230D, AX44, AXJ530, and MRI153M alloys was observed. MRI230D has a higher level of Al and Ca in the primary α-Mg phase, while only a higher level of Al is observed in MRI153M, compared with AX44 and AXJ530. While the increased levels of Al in the MRI alloys may be due in part to higher bulk Al concentrations, the higher level of Ca in the primary phase of MRI230D is attributable to the presence of Sn in this alloy. The differences in the partitioning of Al and Ca to the primary α-Mg phase during solidification influence both solid solution and precipitation strengthening, which can explain observed differences in creep behavior.

DOI: 10.1007/s11661-010-0271-x

I. INTRODUCTION

WITH emphasis on vehicle weight reduction in the automotive industry, interest has grown in magnesium alloys with improved creep resistance. In order to extend the use of Mg alloys to higher temperature powertrain applications, which typically operate in a temperature regime of 423 K to 473 K (150 °C to 200 °C),[1–3] it is necessary to improve the creep resistance of current alloys or develop new Mg alloys with higher creep resistance at elevated temperatures. Powertrain applications typically require cast Mg alloys, for which the creep properties are sensitive to both the solidification path and casting process parameters.

The Mg-Al-Ca system has shown good potential for use in automotive powertrain applications and has been the focus of a number of recent studies.[3–19] Additions of Al and Ca can contribute to both solid-solution and precipitation strengthening.[8,9] In this ternary system, several intermetallic eutectic phases have been identified, depending on the composition of the alloy: β-$Mg_{17}Al_{12}$, Mg_2Ca (C14), and $(Mg,Al)_2Ca$ (C36).[10–12] The C36 phase, due to its higher morphological stability during high-temperature exposure compared to the C14 and β phases, is associated with improved creep properties.[13] Furthermore, Suzuki *et al.* have shown that addition of greater than 1 wt pct Sr indirectly improves the solid solution strengthening of Mg-5Al-3Ca alloys by increasing the Al solute content in the primary α-Mg.[8,12] Die-cast AXJ530 can also be precipitation strengthened with short-term aging treatments, where precipitates of Al_2Ca form parallel to the basal plane. These precipitates can reduce the minimum creep rate in die-cast alloys by a factor of 1.5.[9,12] In permanent mold-cast AXJ530, precipitation strengthening by Al_2Ca can lower the minimum creep rate by an order of magnitude.[14,15] Suzuki *et al.* also reported that elements that form Mg-rich eutectic compounds (which includes Si, Sn, and Ga) have the potential to increase the solid-solution strengthening of the primary α-Mg phase.[8] These Mg-rich compounds are leaner in Al and Ca, permitting these elements to either remain in solid solution or form precipitates during high-temperature exposure.

As most Mg alloys targeted for powertrain applications will be used in the as-cast state, it is important to understand the elemental partitioning that occurs during solidification of the alloy and its influence on high-temperature strengthening mechanisms. In these alloys, a compositional variation across a dendrite or cell results from redistribution of the solute during solidification.[20,21] The first α-Mg that forms from the melt is solute lean and further solute enrichment that occurs during solidification leads to precipitation of intermetallic phases in the interdendritic regions. If no appreciable back diffusion occurs in the solid, the solute is inhomogeneously distributed across the dendrite or cell.[21]

The segregation of solute during solidification can be modeled using the Scheil equation for nonequilibrium solidification:

$$C_s = kC_0(1 - f_s)^{(k-1)} \quad [1]$$

where C_s is the composition of the solid, C_0 is the bulk composition, k is the partitioning coefficient, and f_s is

JESSICA R. TERBUSH, Graduate Student, and J. WAYNE JONES, Professor, are with the Department of Materials Science & Engineering, University of Michigan, Ann Arbor, MI 48109. Contact e-mail: jterbush@umich.edu NICHOLAS D. SADDOCK, formerly Graduate Student, Materials Science and Engineering Department, University of Michigan, is with Allegheny Teledyne, Monroe, NC 28111. TRESA M. POLLOCK, Professor, formerly with the Materials Science and Engineering Department, University of Michigan, is with the Materials Department, University of California, Santa Barbara, CA 93106.

Manuscript submitted January 15, 2009.
Article published online June 22, 2010

the fraction solid.[22,23] The partitioning coefficient, k, is defined as C_s/C_L, where C_L is the composition of the liquid. Elements with a $k > 1$ segregate to the dendrite (cell) core, while elements with a $k < 1$ segregate to the interdendritic region during solidification. Elements with $k \approx 1$ will not strongly segregate during solidification.

Segregation in Mg-based alloys has been studied *via* directional solidification.[24–28] The resulting microstructure depends strongly on the withdrawal rate used during directional solidification, since this controls the cooling rate of the alloy.[25] Many of these directional solidification studies have been undertaken as part of a larger study of the thermodynamic equilibrium in Mg alloy systems. Zhang *et al.* studied microsegregation in binary Mg-4Al, as well as in Mg-Al-Ca alloys such as Mg-5Al-3Ca and AXJ530.[24,25] For these alloys, the Al concentration was found to increase gradually as solidification progressed until the formation of eutectic near the end of solidification, where an abrupt increase in Al concentration was observed. This was true whether the eutectic contained β-$Mg_{17}Al_{12}$ as in binary Mg-4Al[25] or $(Mg,Al)_2Ca$ (C36) as in AXJ530.[24] For the Ca-containing alloys, Zhang *et al.* also found that the concentration of Ca in the primary α-Mg was negligibly small.[24] Mirkovic and Schmid-Fetzer have also analyzed microsegregation in AZ31 and AM50 castings produced by directional solidification.[26–28] In these alloys, Al and Zn both segregate to the interdendritic region, while Mn segregated to the dendrite cores. Mirkovic and Schmid-Fetzer found no significant impact of cooling rate on the Al distribution,[27] while Zhang *et al.* found a slight dependence on withdrawal rate, where the fastest withdrawal rate had slightly lower Al concentration.[25] Mirkovic and Schmid-Fetzer observed an effect of furnace temperature, however, which they attributed to a larger loss of Al at high temperatures.[27] Both Zhang *et al.* and Mirkovic and Schmid-Fetzer report significant discrepancies between their experimental results and the calculated Scheil model, due to back diffusion in the solid during solidification of the alloys.[24–28]

Microsegregation has been studied to a lesser extent in nondirectionally solidified Mg castings. It is important, however, to understand elemental partitioning in specimens that have not been directionally solidified, since most components used in practical applications fall into this category. Suzuki *et al.* studied the effect of Sr additions on partitioning in Mg-5Al-3(Ca,Sr) alloys, and found that Sr additions of greater than 1 wt pct increased the partitioning of Al to the primary α-Mg phase. This increased Al partitioning led to the formation of the $Mg_{17}Sr_2$ phase as a major eutectic component.[8] As Zhang *et al.*[24] note, however, basic microsegregation information is lacking for most Mg alloys, especially compared to Al alloys.

This study focuses on the possible influence of microsegregation on creep properties in Ca-containing alloys. In a previous study,[17] the creep behavior of three die-cast Mg-Al-Ca-based alloys (AXJ530, MRI230D, and MRI153M) was investigated. The composition of these alloys, as determined by ICP, is given in Table I and overlaid on the Mg-rich corner of the Mg-Al-Ca liquidus projection developed by Suzuki *et al.*[11] (Figure 1). The Al concentration ranges from ~5 wt pct in AXJ530 to ~8 wt pct in MRI153M, while the concentration of Ca varies from ~3 to ~1 wt pct, respectively. MRI230D also contains ~0.8 wt pct Sn. All three alloys fall into a compositional region (Figure 1) where formation of the C36 $(Mg,Al)_2Ca$ intermetallic phase by a eutectic reaction is expected. The creep behavior of these die-cast alloys are summarized in Figure 2 for creep at 110 MPa for 373 K and 453 K (100 °C and 180 °C), which are relevant conditions for powertrain applications. Minimum creep rates for test durations up to 500 hours are listed in Table II. While MRI230D and AXJ530 have similar minimum creep rates that differ only by a factor of 1.5 to 2 for the temperature and stress conditions examined, the creep rate for MRI153M is 1 to 2 orders of magnitude higher than that for MRI230D or AXJ530.

There are several possible reasons for the observed differences in creep behavior.[17] The microstructures of the alloys, shown in Figure 3, consist of cells of primary α-Mg surrounded by eutectic phases in the interdendritic regions, and as expected, the predominant eutectic phase is C36. Furthermore, the average cell size is approximately 11 μm for all three alloys, while the grain size is typically on the order of 20 μm for die-cast Mg-Al-Ca alloys.[15] Thus, the variation in creep resistance could not be attributed to differences in microstructure. Dislocation substructures of crept samples of the three alloys were also examined.[17] At both 373 K (100 °C) and 453 K (180 °C), the majority of the dislocations present were identified as basal $\langle a \rangle$ type dislocations,

Table I. Composition of the Cast Alloys in Weight Percent

Alloy	Mg	Al	Ca	Mn	Sr	Zn	Sn
AX44	bal	3.8	3.5	0.01	—	—	—
AXJ530	bal	4.81	3.02	0.30	0.17	<0.01	<0.01
MRI230D	bal	6.45	2.25	0.27	0.25	<0.01	0.84
MRI153M	bal	7.95	0.98	0.20	0.27	<0.01	<0.01

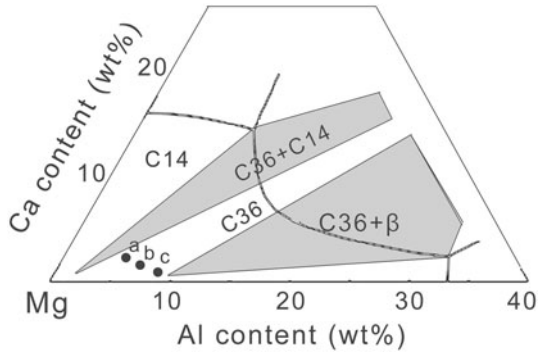

Fig. 1—Liquidus projection of the Mg-rich corner of the Mg-Al-Ca system with expected eutectic compounds labeled.[11] Approximate compositions indicated are (*a*) AXJ530, (*b*) MRI230D, and (*c*) MRI153M.

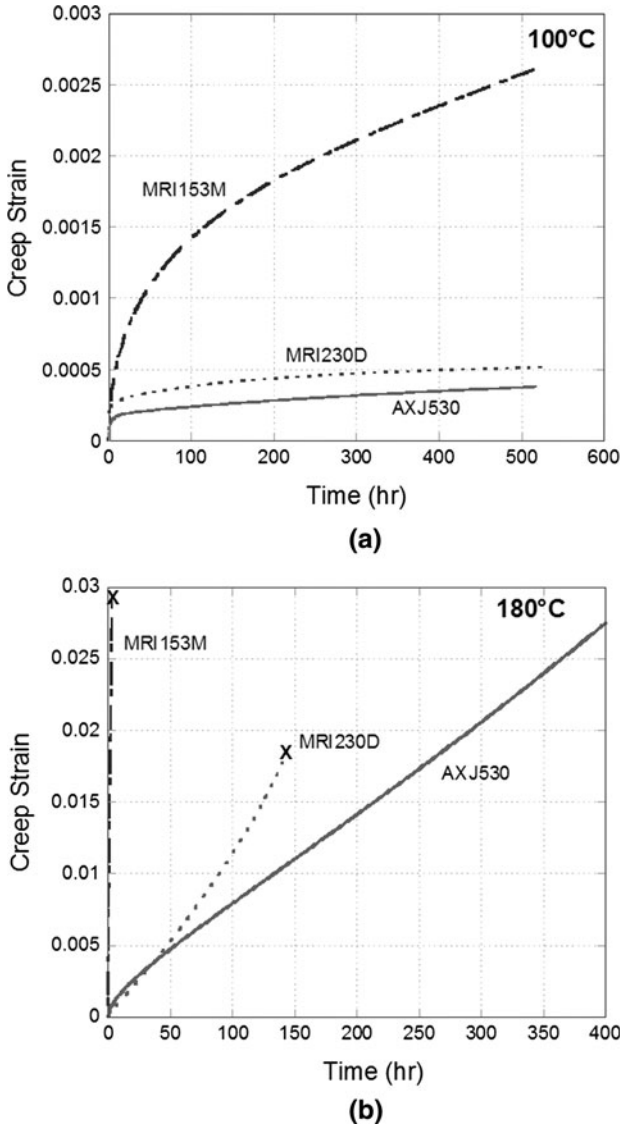

Fig. 2—Tensile creep behavior of AXJ530, MRI153M, and MRI230D, crept at 110 MPa at (*a*) 373 K (100 °C) and (*b*) 453 K (180 °C). Failed specimens are indicated by an *x*.

Table II. Minimum Creep Rate (s^{-1}) after 500 Hours at 110 MPa

Alloy	373 K (100 °C)	453 K (180 °C)
AXJ530	6.68×10^{-11}	1.71×10^{-8}
MRI230D	3.70×10^{-11}	2.73×10^{-8}
MRI153M	6.08×10^{-10}	1.21×10^{-6}

with a significantly lower density of nonbasal $\langle a \rangle$ and $\langle c + a \rangle$ dislocations also present at the higher temperature. Viscous glide on basal planes was identified as the predominant creep deformation mechanism. Therefore, differences in creep resistance could not be attributed to a difference in operative creep deformation mechanism. The aging behavior of the three alloys was subsequently examined to infer any differences in primary α-Mg composition for the three alloys.[18] Differences in the precipitation behavior were observed upon aging; in aged AXJ530 and MRI230D, basal precipitates of Al_2Ca form in the cell interior, while blocky precipitates of β-$Mg_{17}Al_{12}$ form in the near-boundary region in aged MRI153M, suggesting that compositional differences in the primary α-Mg do indeed exist in the three alloys and may contribute to the observed differences in creep resistance.

The objective of the present study is to quantify the partitioning of elements to the primary alpha phase during solidification and the dependence of partitioning on alloy composition to better understand the potential for solid solution or precipitation strengthening of the α-Mg phase in Mg-Al-Ca alloys, with the ultimate goal of identifying possible alloying strategies for improved creep resistance. Ternary and quaternary alloys have been studied to evaluate a range of potential alloying additions.

II. EXPERIMENTAL PROCEDURE

Permanent mold cast specimens of four alloys, MRI230D, MRI153M, AXJ530, and AX44, were prepared. Small castings weighing 25 g were prepared from MRI230D and MRI153M ingots supplied by Dead Sea Magnesium. The samples were melted in an induction furnace using a mild steel crucible under a cover gas of 1 pct SF_6 in argon and then recast into an unheated low-carbon steel mold. This produced a sufficiently slow solidification rate of ~3 to 5 K/s to achieve an average primary α-Mg cell size of approximately 20 μm (Figure 4). This cell size was a factor of 10 larger than the electron beam spot size and sufficient to decrease the likelihood of sampling both α-Mg and eutectic phases during a single microprobe measurement.

Samples of AXJ530 and AX44 (Mg-4Al-4Ca) were permanent mold cast from ingots supplied by General Motors and Norsk Hydro, respectively. The alloys were melted in a Striko-Dynarad resistance furnace in an uncoated mild steel crucible and poured into a preheated permanent steel mold coated with boron nitride. A cover gas of 0.5 vol pct SF_6, 25 vol pct CO_2, and a balance of dry air was used during casting. The mold temperature increased from 473 K to 673 K (200 °C to 400 °C) during the course of the casting run. Cooling rates of ~10 K/s were observed, and average cell sizes of 22 μm for AXJ530 and 18 μm for AX44 were produced.[14,19] Metallographic sections of all as-cast alloys were given a final polish with 0.25-μm diamond paste on a neoprene pad prior to microprobe examination.

A CAMECA (Gennevilliers, France) SX100 electron microprobe analyzer (EMPA) was used for composition measurements, following the procedure previously described.[29–31] A voltage of 20 kV and beam current of 15 nA was used. Area scans with a square grid of 400 to 900 sampling points were collected from regions with representative microstructure, with a step size of 10 to 15 μm between points. The standards used for each element are identified in Table III.

The Mg concentration will vary from the cell interior to the near-boundary region as a result of partitioning

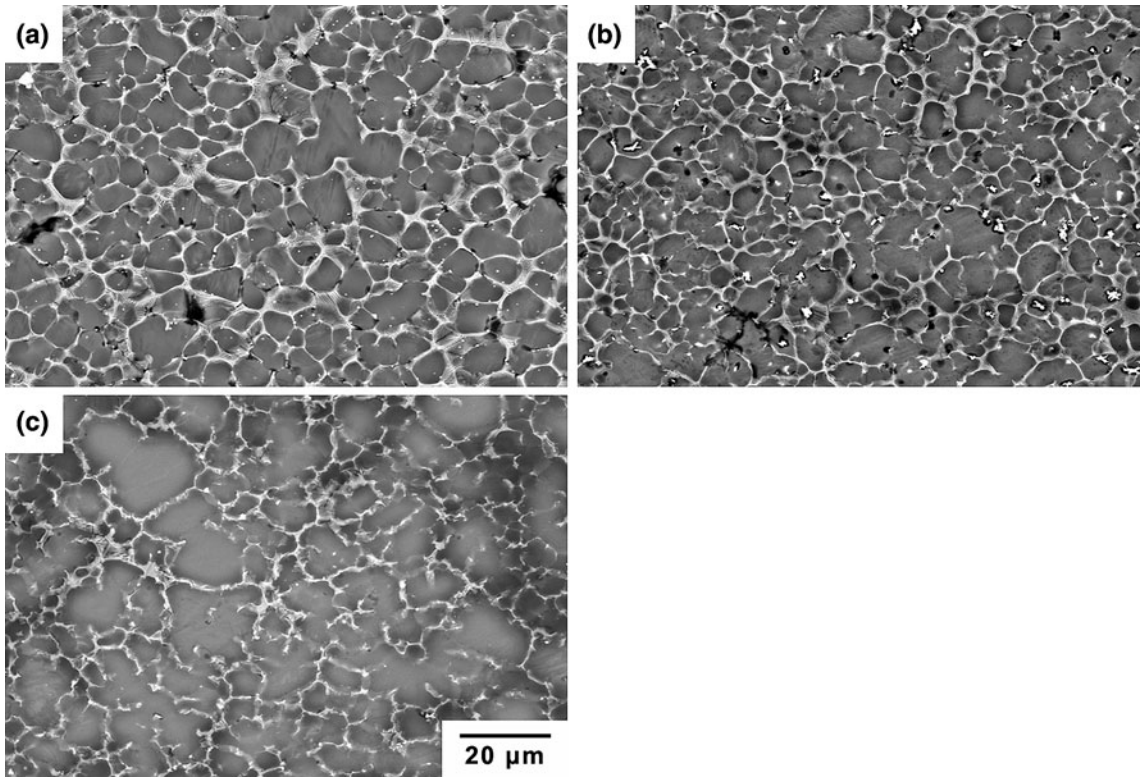

Fig. 3—SEM (BSE) images of die-cast (*a*) AXJ530, (*b*) MRI230D, and (*c*) MRI153M. All samples were etched for 5 s prior to imaging. The darker gray regions are cells of primary α-Mg, while the brighter contrast features are intermetallic phases in the eutectic.

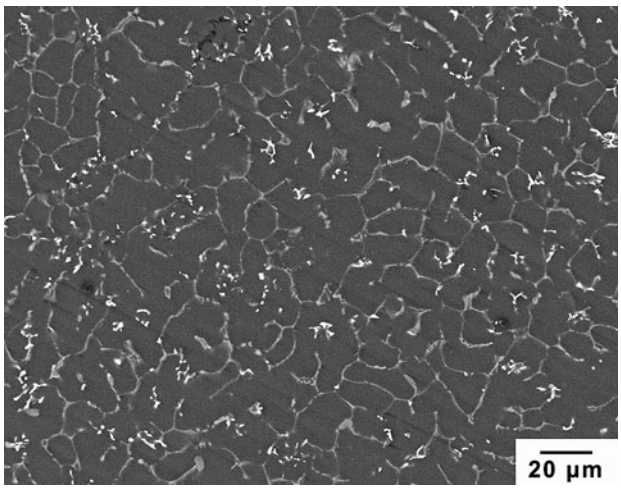

Fig. 4—SEM (BSE) image of recast MRI230D, unetched. The dark gray regions are cells of primary α-Mg, while the medium gray contrast is the C36 $(Mg,Al)_2Ca$ phase. The bright white features are a Ca-Sn intermetallic phase.

during solidification. Based on the binary phase diagrams, the first solid that forms will have the highest Mg concentration and the last point to solidify will have the lowest. Accordingly, the raw data generated by the EMPA was sorted in decreasing order of Mg concentration, since primary α-Mg is the first phase to form during solidification. Using this scheme, an apparent fraction solid can be determined based on the Mg concentration at each collection point, and the concentration of selected elements can be plotted against this apparent fraction solid to show the compositional variation during solidification of the alloy.

Table III. Electron Microprobe Standards

Element (Line)	Standard
Mg (K_α)	homogenized Mg-4Al
Al (K_α)	100 pct Al
Ca (K_α)	Wollastonite (34.2 pct Ca)
Mn (K_α)	BHRH (29.27 pct Mn)
Zn (K_α)	100 pct Zn
Sr (L_α)	Celestite (47.7 pct Sr)
Sn (L_α)	100 pct Sn
O (K_α)	SiO_2 (53.3 pct O)

III. RESULTS AND DISCUSSION

The segregation profiles of the three major elements (Mg, Al, and Ca) are shown in Figure 5 for the recast samples of MRI230D and MRI153M and the permanent mold cast AXJ530 and AX44. AX44 is included as a baseline for comparison of an Mg-Al-Ca–based alloy containing no major quaternary additions. The Al segregation profiles, shown in Figure 5(b), are especially of interest, since Al can contribute to both solid solution and precipitation strengthening in Mg alloys.[8,9,32] However, it is not possible to distinguish between the

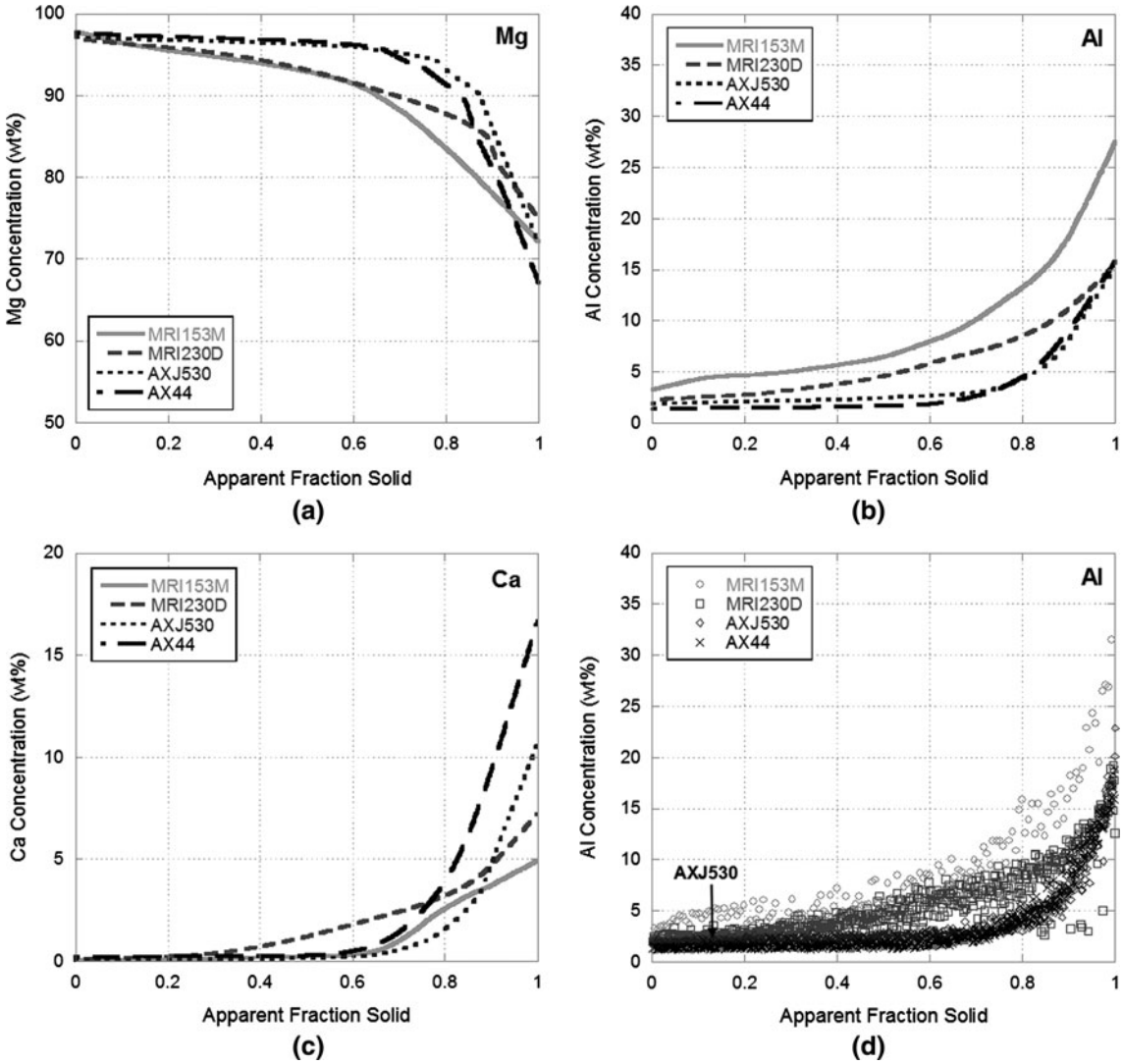

Fig. 5—Least-mean-squares fit of concentration profiles for (*a*) Mg, (*b*) Al, and (*c*) Ca in MRI153M, MRI230D, AXJ530, and AX44, as measured by the electron microprobe. (*d*) Same as (b), except showing the scatter in the experimental data, which is caused by errors in the Mg concentrations used to sort the rest of the elements.

two forms of strengthening with compositional measurements alone since the electron beam will sample both the matrix and any nanometer-scale precipitates present. In Figure 5(b), AX44 and AXJ530 have similar levels of Al in the primary α-Mg, while MRI230D and MRI153M both have higher levels of Al. Part of this difference may result from the higher bulk concentration of Al in the two MRI alloys, 6.5 to 8 wt pct as compared to the 4 to 5 wt pct in AX44 and AXJ530, respectively. However, it is also interesting to note that for the MRI230D, the shape of the Al segregation profile differs from the Al segregation profiles of the other three alloys. This will be discussed in more detail later.

The Ca segregation profile is shown in Figure 5(c). Ca has a lower solubility than Al in Mg, but its larger atomic misfit could still give rise to solid solution strengthening.[33,34] The Ca may also contribute to precipitation strengthening; for example, precipitates of Al_2Ca have been observed in aged samples of AXJ530[9,18] and MRI230D.[18] In Figure 5(c), the Ca profiles of MRI153M, AX44, and AXJ530 are fairly similar. Significantly more Ca was present in the primary α-Mg of the MRI230D. This is in spite of the fact that MRI230D has a lower bulk Ca concentration than either AX44 or AXJ530. As observed for Al, the Ca segregation profile for MRI230D is different from that observed for the other three alloys.

A Scheil equation was fit to the experimental data from the microprobe and is shown in Figure 6 for the Mg, Al, and Ca concentrations of the recast MRI230D. The fitted Scheil curves do not accurately reflect the experimental data for most of the solidification range. The Scheil equation greatly underestimates the concentration at high fraction solid especially. Also shown in this figure are Scheil segregation curves calculated using the PANDAT* thermodynamic database. The

*PANDAT is a trademark of CompuTherm LLC, Madison, WI.

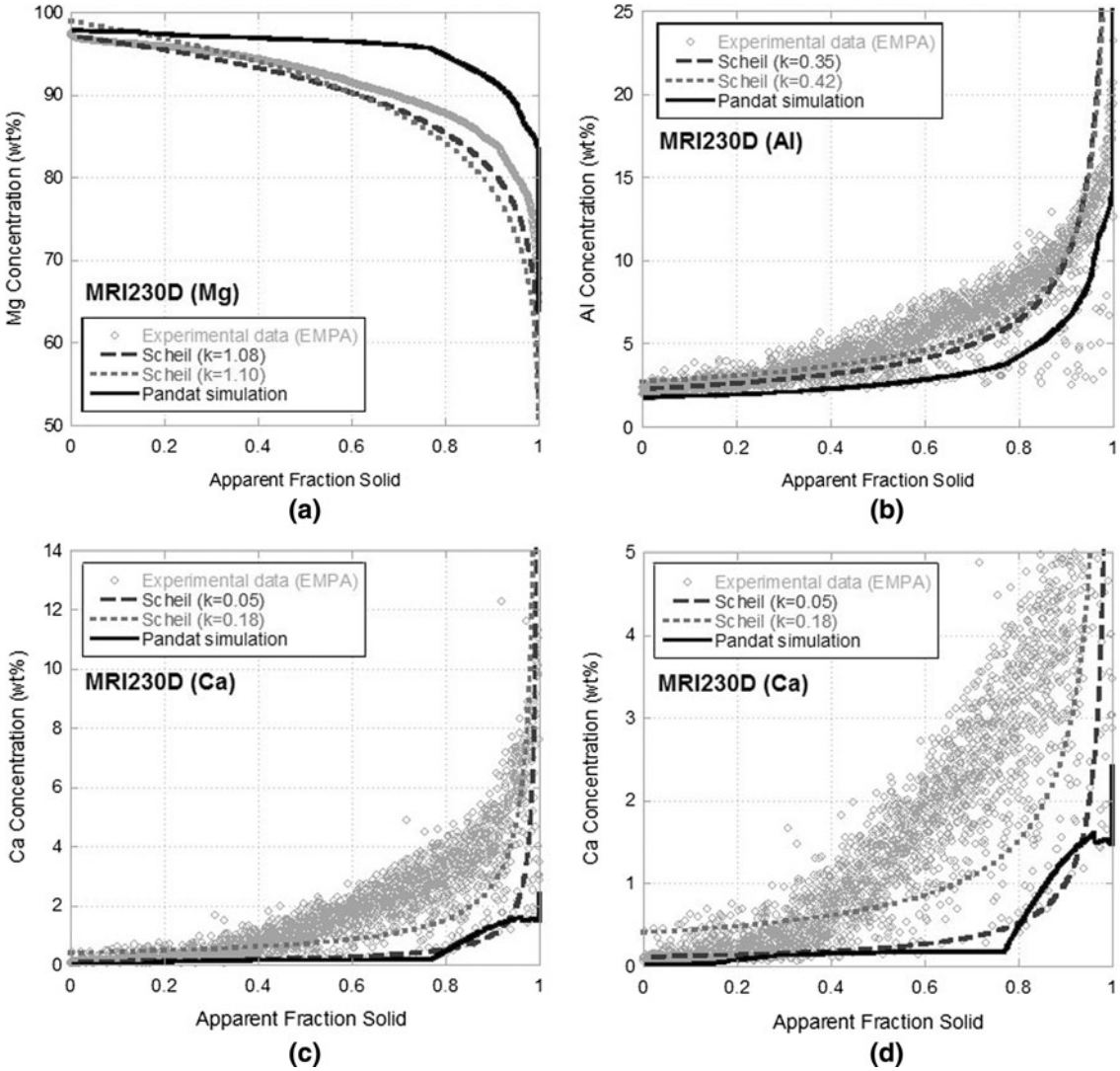

Fig. 6—Comparison of experimental data, predicted Scheil (from PANDAT), and fitted Scheil curves for recast MRI230D for (*a*) Mg, (*b*) Al, (*c*) Ca, and (*d*) same as (c), but focused on smaller concentrations to clearly show the prediction from PANDAT.

Table IV. Scheil Partitioning Coefficients

Alloy	k_{Mg}	k_{Al}	k_{Ca}
AX44	1.05	0.32	0.05
AXJ530	1.03	0.38	0.06
MRI230D (0 to 10 pct)	1.08	0.35	0.05
MRI230D (10 to 60 pct)	1.10	0.42	0.18
MRI153M	1.07	0.50	0.06

PANDAT curves, while fairly similar to the experimental data for the first part of solidification, also underestimate the amount of Al and Ca for larger fraction solid. Curvature in the phase field boundaries can lead to nonlinear variation in both C_s and C_L and, thus, changes in the partitioning coefficient. Back diffusion in the solid can also change the shape of the segregation profile, and the Scheil equation does not account for this.

The partitioning coefficients determined from the fit of the segregation data for the major elements of MRI230D and the other alloys are summarized in Table IV. Two sets of values are included for MRI230D. The first are average coefficients that were determined using the first 10 pct to solidify; thus, the fit is not as good at high fraction solid (Figure 6). Based on the overall shape of the segregation curve for MRI230D compared to AX44 and AXJ530, one would expect the k values for both Al and Ca to be significantly different for MRI230D. In particular, the Ca partitioning coefficient is expected to be highest for MRI230D given the segregation profile. However, the partitioning coefficients calculated with this first method are actually very similar, suggesting that for the first solid to form, segregation is fairly similar for these alloys. If the later stages of solidification are considered, from 10 to 60 pct solidified, partitioning is much stronger in MRI230D. However, higher k values that reflect this stronger partitioning do not capture the shape of the entire segregation profile in Figure 6. For the recast MRI153M, the calculated Al partitioning coefficient is

higher and the Ca partitioning coefficient is approximately the same as that of AX44 and AXJ530. This is expected, based on the shape of the segregation profile for MRI153M.

The variation in partitioning to the primary α-Mg in AXJ530, MRI230D, and MRI153M may explain the differences in creep behavior observed in these alloys. Increased solute can lead to increased solid solution strengthening during creep. Saddock has calculated that the influence of solute alone can account for differences in creep rate of up to three orders of magnitude.[15] In a recent study by Zhu *et al.*,[35] the creep resistance of die-cast Mg-4Al-2RE was reported to be related to the amount of Al solute in the primary α-Mg after casting. When creep is controlled by viscous glide (as it is for the alloys currently under investigation), Mohamed and Langdon[33] have proposed the following model relating creep rate, $\dot{\varepsilon}$, to solute concentration:

$$\dot{\varepsilon} \approx \frac{\pi(1-\nu)\mathrm{k}T\tilde{D}}{6e^2c\mathbf{b}^5G}\left(\frac{\sigma}{G}\right)^3 \qquad [2]$$

where ν is Poisson's ratio, σ is the applied stress, k is Boltzmann's constant, T is the absolute temperature, $\tilde{D}$ is the interdiffusion coefficient for the solute, G is the shear modulus, $\mathbf{b}$ is the Burgers vector, e is the solute-solvent size difference, and c is the concentration of solute. When comparing the alloys studied, the dependence of the material parameters in Eq. [2] on small changes in composition is negligible with the exception of e, c, and $\tilde{D}$. Thus, these terms can be evaluated to estimate the influence of solute concentration on creep, and the alloy with the largest $\frac{e^2c}{\tilde{D}}$ would be expected to have the lowest creep rate. However, since the interdiffusion coefficients are not known for most of the elements in this complex alloy system, only e^2c will be considered at this time. The diffusivity of Al and Ca may be greatly different, however, so the contribution from the elements will not have equal weight.

The values of e^2c for Al and Ca are included in Table V for the four alloys studied. The atomic misfit (e) of Al in Mg is −12.4 and 20.4 pct for Ca in Mg.[36] The solute concentrations used for this calculation are approximations taken from the near boundary region of the microstructure, which corresponds to a fraction solid of ~0.7. The Al and Ca concentrations in the α-Mg will be near maximum in this region based on the shape of the segregation curves, and PANDAT simulations predict that eutectic phases will start to form at a fraction solid of just over 0.75. Based on the solute contributions in Table V, one would expect MRI153M to have a low creep rate; however, this fails to take into account any precipitation that occurs at creep temperatures.

Table V. Contribution of Solute Concentration to Creep

	Al		Ca	
Alloy	c (Wt Pct)	e^2c	c (Wt Pct)	e^2c
AX44	3.3	507	2.1	874
AXJ530	4.1	630	1.3	541
MRI230D	7.2	1107	2.7	1124
MRI153M	11.6	1784	1.5	624

Suzuki *et al.* suggested that by increasing the solid solubility of Ca in the α-Mg matrix of Mg-Al-Ca–based alloys at elevated temperatures, the volume fraction of precipitates present can be increased to improve the precipitation strengthening of the alloy.[9] MRI230D has high levels of both Al and Ca, and during exposure to high temperatures, precipitates of Al_2Ca can form in the cell interiors, as observed in our previous aging study.[18] For MRI153M, however, while the level of Al in the primary phase is as high as in MRI230D, the Ca concentration is much lower. Thus, precipitates of Al_2Ca are unlikely to form in the cell interiors. In the near-boundary region, the Al concentration of MRI153M exceeds the equilibrium amount of Al that can be dissolved in Mg, about 12.9 wt pct according to the binary Mg-Al phase diagram.[37] Thus, precipitates of β-$Mg_{17}Al_{12}$ may form in this region, which is again supported by our previous aging study.[18] Although automotive alloys are mostly used in the as-cast condition, they are still subjected to long-term thermal exposure during use, and it is important to consider the precipitates that may form. Alloys such as AXJ530 and MRI230D that retain sufficient Al in the primary phase to avoid the formation of β-$Mg_{17}Al_{12}$ during high-temperature exposure and which also have sufficient Ca available for precipitate formation offer a viable approach to improving creep resistance in Mg-Al–based alloys.

The presence of Sn in MRI230D may account for the difference in partitioning during solidification that is observed in this alloy. It is interesting to note that AX44, AXJ530, and MRI153M, which do not contain Sn, have very similar concentration profiles, with the increased Al in the primary phase of the MRI153M most likely due to the higher bulk Al concentration in this alloy. The presence of Sn in MRI230D also may affect the diffusion and solubility of the other alloying elements, increasing the amount of Al and Ca that remain in the primary phase. At this time, the lack of diffusion data for these complex systems makes it difficult to draw a definitive conclusion. However, compared to AXJ530, slower Al_2Ca aging kinetics were observed for MRI230D, indicating that Sn can affect interdiffusion in this alloy.[18] As illustrated in Figure 7, the presence of Sn can also change the solidification path of the alloy. In this figure, the calculated solidification paths for AX44 and Mg-6.5Al-2.25Ca (the ternary composition of MRI230D) are shown; with the addition of Sn to the MRI230D base composition, the solidification path may be modified to more closely resemble the dotted line. Ongoing studies on quaternary Mg-5Al-3Ca-xSn alloys indicate that Sn additions of 0.75 wt pct result in a segregation profile similar to that of MRI230D, supporting the suggested change in solidification path. As further confirmation, current studies are underway to examine the effect of adding Sn to the MRI153M base composition and removing Sn from MRI230D on microsegregation and creep in these alloys. These results will be reported in more detail in the future.

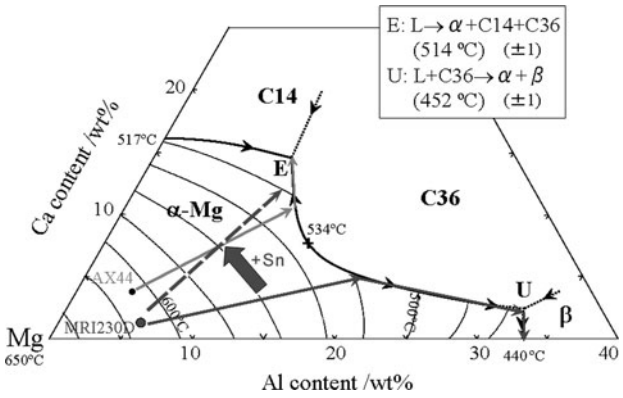

Fig. 7—Mg-Al-Ca liquidus projection,[11] showing the solidification path for AX44 and the ternary composition of MRI230D (*i.e.*, Mg-6.5Al-2.25Ca). The dotted line indicates a potential solidification path after Sn addition.

IV. CONCLUSIONS

The partitioning of elements to the primary α-Mg phase has been studied for four Mg-Al-Ca–based alloys using electron microprobe analysis. Sn additions change the solidification path, as observed in MRI230D. Samples of MRI230D and MRI153M had higher levels of Al in the primary alpha phase than AX44 or AXJ530, due at least in part to their higher bulk Al concentration. However, MRI230D also had increased levels of Ca in the primary alpha phase despite its lower bulk Ca concentration. This variation in partitioning to the primary phase can also explain the aging behavior observed in these alloys.

ACKNOWLEDGMENTS

The authors acknowledge the support of the National Science Foundation FRG, Grant Nos. F015408 and DMR-0309468. We also thank J. Zhu, R. Adharapurapu, C. Torbet, and C. Henderson, University of Michigan, for their assistance; A. Suzuki, GE Global Research, for her advice; and B.R. Powell, General Motors, for his many helpful discussions.

REFERENCES

1. M.O. Pekguleryuz and E. Baril: *Mater. Trans.*, 2001, vol. 42, pp. 1258–67.
2. P. Bakke, H. Westengen, S. Sannes, and D. Albright: *SAE 2004 World Congr., Vol. 2004-01-0655*, SAE International, Detroit, MI, 2004.
3. A.A. Luo: *Int. Mater. Rev.*, 2004, vol. 49, pp. 13–30.
4. Y. Mori, Y. Terada, and T. Sato: *Mater. Trans.*, 2005, vol. 46, pp. 1747–52.
5. A.A. Luo, M.P. Balogh, and B.R. Powell: *Metall. Mater. Trans. A*, 2002, vol. 33A, pp. 567–74.
6. Y. Terada, N. Ishimatsu, and T. Sato: *Mater. Trans.*, 2007, vol. 48, pp. 2329–35.
7. Y. Terada, R. Sota, N. Ishimatsu, T. Sato, and K. Ohori: *Metall. Mater. Trans. A*, 2004, vol. 35A, pp. 3029–32.
8. A. Suzuki, N.D. Saddock, L. Riester, E. Lara-Curzio, J.W. Jones, and T.M. Pollock: *Metall. Mater. Trans. A*, 2007, vol. 38A, pp. 420–27.
9. A. Suzuki, N.D. Saddock, J.R. TerBush, B.R. Powell, J.W. Jones, and T.M. Pollock: *Metall. Mater. Trans. A*, 2008, vol. 39A, pp. 696–702.
10. A. Suzuki, N.D. Saddock, J.W. Jones, and T.M. Pollock: *Scripta Mater.*, 2004, vol. 51, pp. 1005–10.
11. A. Suzuki, N.D. Saddock, J.W. Jones, and T.M. Pollock: *Acta Mater.*, 2005, vol. 53, pp. 2823–34.
12. A. Suzuki, N.D. Saddock, J.R. TerBush, B.R. Powell, J.W. Jones, and T.M. Pollock: in *2007 SAE World Congr., Vol. 2007-01-1025*, SAE International, Detroit, MI, 2007.
13. A. Suzuki, N.D. Saddock, J.W. Jones, and T.M. Pollock: *Metall. Mater. Trans. A*, 2006, vol. 37A, pp. 975–83.
14. N.D. Saddock, A. Suzuki, J.R. TerBush, J.W. Jones, T.M. Pollock, J.E. Zindel, and J.E. Allison: *2007 SAE World Congress, Vol. 2007-01-1027*, SAE International, Detroit, MI, 2007.
15. N.D. Saddock: Ph.D. Thesis, University of Michigan, Ann Arbor, MI, 2007.
16. N.D. Saddock, A. Suzuki, J.R. TerBush, J.W. Jones, and T.M. Pollock: in *Magnesium Technology 2007*, R.S. Beals, A.A. Luo, N.R. Neelameggham, and M.O. Pekguleryuz, eds., TMS, Warrendale, PA, 2007, pp. 407–12.
17. J.R. TerBush, A. Suzuki, N.D. Saddock, J.W. Jones, and T.M. Pollock: *Scripta Mater.*, 2008, vol. 58, pp. 914–17.
18. J.R. TerBush, J.W. Jones, and T.M. Pollock: in *Magnesium Technology 2008*, M.O. Pekguleryuz, N.R. Neelameggham, R.S. Beals, and E.A. Nyberg, eds., TMS, Warrendale, PA, 2008, pp. 117–22.
19. N.D. Saddock, A. Suzuki, J.R. TerBush, E.C. Heininger, J. Zindel, J.E. Allison, T.M. Pollock, and J.W. Jones: in *Magnesium Technology 2006*, A.A. Luo, N.R. Neelameggham, and R.S. Beals, eds., TMS, Warrendale, PA, 2006, pp. 77–82.
20. Y.M. Won and B.G. Thomas: *Metall. Mater. Trans. A*, 2001, vol. 32A, pp. 1755–67.
21. D.A. Porter and K.E. Easterling: *Phase Transformations in Metals and Alloys*, 2nd ed., Nelson Thornes Ltd., Cheltenham, 1992, pp. 185–262.
22. H.D. Brody and M.C. Flemings: *Trans. TMS-AIME*, 1966, vol. 236, pp. 615–24.
23. T.F. Bower, H.D. Brody, and M.C. Flemings: *Trans. TMS-AIME*, 1966, vol. 236, pp. 624–34.
24. C. Zhang, D. Ma, K. Wu, H. Cao, J. Zhu, G. Cao, S. Kou, and Y.A. Chang: in *Magnesium Technology 2006*, A.A. Luo, N.R. Neelameggham, and R.S. Beals, eds., TMS, Warrendale, PA, 2006, pp. 45–50.
25. C. Zhang, D. Ma, K.-S. Wu, H.-B. Cao, G.-P. Cao, S. Kou, Y.A. Chang, and X.-Y. Yan: *Intermetallics*, 2007, vol. 15, pp. 1395–1400.
26. D. Mirkovic and R. Schmid-Fetzer: *Metall. Mater. Trans. A*, 2009, vol. 40A, pp. 958–73.
27. D. Mirkovic and R. Schmid-Fetzer: *Metall. Mater. Trans. A*, 2009, vol. 40A, pp. 974–81.
28. D. Mirkovic and R. Schmid-Fetzer: in *Magnesium Technology 2009*, E.A. Nyberg, S.R. Agnew, N.R. Neelameggham, and M.O. Pekguleryuz, eds., TMS, Warrendale, PA, 2009, pp. 97–100.
29. M. Gungor: *Metall. Trans. A*, 1989, vol. 20A, pp. 2529–33.
30. S.C. Huang, L. Peluso, and D. Backman: in *Solidification*, W.H. Hofmeister, J.R. Rogers, N.B. Singh, S.P. Marsh, and P.W. Vorhees, eds., TMS, Warrendale, PA, 1999, pp. 163–72.
31. S. Tin, T.M. Pollock, and W. Murphy: *Metall. Mater. Trans. A*, 2001, vol. 32A, pp. 1743–53.
32. M.S. Dargusch, K. Pettersen, K. Nogita, M.D. Nave, and G.L. Dunlop: *Mater. Trans.*, 2006, vol. 47, pp. 977–82.
33. F.A. Mohamed and T.G. Langdon: *Acta Metall.*, 1974, vol. 22, pp. 779–88.
34. K. Maruyama, M. Suzuki, and H. Sato: *Metall. Mater. Trans. A*, 2002, vol. 33A, pp. 875–82.
35. S.M. Zhu, M.A. Gibson, J.F. Nie, M.A. Easton, and T.B. Abbott: *Scripta Mater.*, 2008, vol. 58, pp. 477–80.
36. T. Uesugi, M. Kohyama, and K. Higashi: *Mater. Sci. Forum*, 2003, vols. 426–432, pp. 599–604.
37. *ASM Handbook, Vol. 3—Alloy Phase Diagrams*, ASM INTERNATIONAL, Metals Park, OH, 1992.